Computational Exploration of Thermodynamic Models of Geological CO_2 Injection

by

Jonathan Edelman

B.S. Mathematics and Computer Science and Engineering, MIT, 2024

Submitted to the Department of Electrical Engineering and Computer Science
in partial fulfillment of the requirements for the degree of

MASTER OF ENGINEERING IN ELECTRICAL ENGINEERING AND COMPUTER SCIENCE

at the

MASSACHUSETTS INSTITUTE OF TECHNOLOGY

May 2025

Authored by: Jonathan Edelman
Department of Electrical Engineering and Computer Science
May 9, 2025

Certified by: Laurent Demanet
Professor of Mathematics, Thesis Supervisor

Accepted by: Katrina LaCurts
Chair
Master of Engineering Thesis Committee

Computational Exploration of Thermodynamic Models of Geological CO_2 Injection

by

Jonathan Edelman

Submitted to the Department of Electrical Engineering and Computer Science
on May 9, 2025 in partial fulfillment of the requirements for the degree of

MASTER OF ENGINEERING IN ELECTRICAL ENGINEERING AND COMPUTER SCIENCE

ABSTRACT

This thesis investigates the behavior of carbon dioxide flow in porous media through high-fidelity computational modeling, with a specific focus on the impact of the Span-Wagner equation of state (EOS). Accurate modeling of CO_2 transport in subsurface environments is essential for applications such as carbon capture and storage (CCS). We model the entire flow from injection, down throughout a vertical pipe and into a porous reservoir. To this end, we utilize the MOOSE (Multiphysics Object-Oriented Simulation Environment) framework developed by Idaho National Laboratory to perform finite element simulations. A key contribution of this work is the successful coupling of a porous rock domain with a one-dimensional pipe flow simulation in Julia, enabling a broader representation of injection scenarios. The study examines how the thermodynamic accuracy of the Span-Wagner Equation of State influences flow characteristics, in comparison to the Ideal Gas Equation of State. Through a series of coupled pipe-reservoir simulations, we assess variations in pressure and density as CO_2 is injected from the pipe into the porous medium. The model can detect phase change conditions, allowing us to predict the maximum mass flux that can be achieved below the liquefaction threshold, as defined by the binodal curve in the CO_2 phase diagram at a given temperature. The results highlight the importance of EOS selection in predicting multiphase flow behavior, especially under conditions relevant to geological storage. Furthermore, we find that the Ideal Gas EOS underpredicts injection rates under the same conditions. This integrated modeling approach advances the understanding of thermodynamic effects in coupled subsurface flow systems and supports the development of reliable tools for large-scale carbon storage applications.

Thesis supervisor: Laurent Demanet
Title: Professor of Mathematics

Acknowledgments

I am deeply grateful to my father, Professor Alan Edelman, whose inspiration and unwavering support led me to pursue my Master's degree.

My sincere thanks to my mother, Dr. Susan Haden, for her constant care and for ensuring that I could focus entirely on my research without distraction.

To my older brother, Daniel Edelman, thank you for the shared meals and the quiet companionship during our time living together—they brought balance to this journey.

I extend my formal appreciation to my younger brother, Professor Philip the Corgi, whose presence and wisdom have been a consistent source of insight and perspective throughout my studies.

To my girlfriend, Emma Fu, thank you for your encouragement and for motivating me through the most challenging phases of this work.

I am truly thankful to my supervisor, Professor Laurent Demanet, for offering me a project that I found deeply engaging and intellectually rewarding.

And to my co-supervisor, Professor Aimé Fournier, I am especially grateful for his steady guidance and weekly meetings, which ensured continual progress and clarity. Additionally, Aime is to be credited for the work in appendices 1.1.1 through 1.1.5 and the description of the pipe simulation, that we reproduce here with permission.

Contents

List of Figures

List of Tables

Chapter 1

Introduction

1.1 Background and Motivation

Modeling fluid flow in porous media is useful for a wide range of applications, including carbon sequestration, oil and gas recovery, and aquifer analysis. Specifically, understanding the flow of gas-phase or supercritical carbon dioxide (CO_2) is essential for carbon capture and storage technologies. When pressure and temperature are applied to carbon dioxide that is captured from the atmosphere, it becomes a supercritical fluid that can then be stored in porous rocks in the ground. These carbon capture and storage (CCS) technologies rely on accurate modeling of fluid flow and storage.

We model the flow of CO_2 throughout the entire flow from the injection site, down through a vertical pipe, and deep into a porous rock reservoir.

One key decision for the model is which Equation of State (EOS) to use to describe the relationship between pressure p, temperature T, and density ρ. Many studies use the Ideal Gas Law as it is a very simple EOS and is easy to implement. However, at high pressures real gases like CO_2 begin to exhibit non-ideal behavior which decreases the accuracy of the Ideal Gas Law. The Span-Wagner EOS is a more accurate relationship between p, ρ and T for CO_2, especially under the high-pressure conditions critical for CCS. However, the cost of the added precision is it takes longer to compute during the simulation.

This thesis investigates how each EOS impacts the CO_2 behavior in a coupled simulation between a vertical pipe and horizontal porous medium. We aim to quantify the differences in model predictions. We find the Ideal Gas Law underestimates the pressure gradient with depth in the pipe, and overestimates the pressure increase in the reservoir. In both cases, this owes to the fact that the Ideal Gas Law systematically underestimates density. To achieve the same bottom pressure in the pipe at a given flow rate, the Span-Wagner EOS predicts a lower required wellhead pressure. Furthermore, for Span-Wagner EOS, the bottom-pipe pressure also can be lowered to achieve the same mass flow rate, since the bottom-pipe pressure increase is proportional to the volumetric flow rate. Both of these effects enhance injectivity, as the same rate can be achieved with lower pressures. Requiring lower pore pressures also reduces the risk of inducing seismicity in the rock.

We developed a flexible and extensible code framework that supports any equation of state (EOS) for one-dimensional pipe flow simulations. This code is designed for seamless integration with reservoir simulations defined in MOOSE input (.i) files.[1]

1.2 Problem Statement

We are interested in modeling the complete flow of carbon dioxide at all locations, from the injection point to deep within the reservoir. The fluid flow down a long vertical pipe from the injection point, and at the bottom of the pipe there is a large porous rock filled with water that the CO_2 permeates through due to the pressure.

We specifically aim to understand how accurate thermodynamic modeling affects predictions of CO_2 flow. To achieve this, we create a simulation that covers a coupling of the pipe and reservoir that is capable of handling multiple EOSes.

The EOS for a gas relates a large number of thermodynamic quantities, and given any two thermodynamic variables, the EOS determines the rest. For our simulations, we care specifically about the relationship between p, ρ and T.

The EOSes we focus on in this study are:

- The Ideal Gas EOS, given by:
$$p = \rho R_s T \tag{1.1}$$

- The Span-Wagner EOS, which provides a more accurate density calculation:
$$\rho = f(p, T), \tag{1.2}$$
where f represents the nonlinear function derived from empirical data and thermodynamic principles.[2]

By solving the governing equations for flow in the coupled pipe and porous medium under these two models, we will assess how the choice of EOS influences predicted pressures, densities, and potential phase changes.

The phase diagram of CO_2 is well studied. It is enough for our simulations to detect if these regimes are encountered without modeling the phase change themselves. We use the binodal curve for CO_2 to identify the region of phase change.

[1]The source code used in this study is available at: https://github.com/JonathanEdelmanS/bluefin. While the repository is not fully documented, it contains the core implementation developed for this thesis.

[2]More information on this EOS can be found in the original Span-Wagner paper in [4]. We plot isotherms in p, ρ for Span-Wagner in 2.1.

Chapter 2

Methods

Variable	Location
x_0	Injection point, i.e. the top of the pipe where depth $z = 0$.
x_1	The linkage point between the pipe and the reservoir, $z = z$ and $r = d/2$.
x_∞	Far end of the reservoir simulation, i.e. $r = \infty$.

Table 2.1: Description of x_0, x_1, x_∞ notation for variable x.

2.1 Simple pipe simulation

Idealized cases serve to build physical understanding and validate numerical simulations. Thus, we start with a very simple model of 1D steady flow, including Mass and Momentum Conservation Laws (A.2) and (A.3). Equations A.7 and A.20 are for a general Equation of State, but initially we assume an Ideal Gas (A.8). Conservation of Energy (A.59) could be included, but would be complicated by consideration of the unknown rate of work of injecting the fluid. Initially we consider either temperature instantly equilibrated with the formation (A.15), or the isothermal case (A.16). The dimensionless numbers to consider are those of Froude, F (A.12), Mach (A.13), Reynolds, R (A.25) and Atwood (A.26).

Although the pipe-top velocity and density u_0 and ρ_0 are mathematically convenient parameters, to connect with operational practice they could be eliminated in favor of 2 given pressures

$$p_0 = p(T_0, \rho_0), \tag{2.1}$$

$$p_1 = p(T(Z), \rho_0 u_0/u(Z)), \tag{2.2}$$

using the Equation of State and Eq. A.4, assuming both pressures are above the spinodal curve[1] $\rho \mapsto p$ defined by $(\partial p/\partial \rho)_T = 0$. Alternatively, one could make p a primary variable instead of ρ (Section A.1.4).

We can also replace viscous drag $\rho^{-1}\mu\frac{\partial^2 u}{\partial z^2}$ with the Darcy–Weisbach friction model $-fu^2$ (Section A.1.3), which eliminates one boundary condition.

[1] E.g., for the usual van der Waals parameters (a, b), the spinodal curve is $\rho \mapsto a\rho^2 - 2ab\rho^3 \xrightarrow{\text{ideal gas}} 0$.

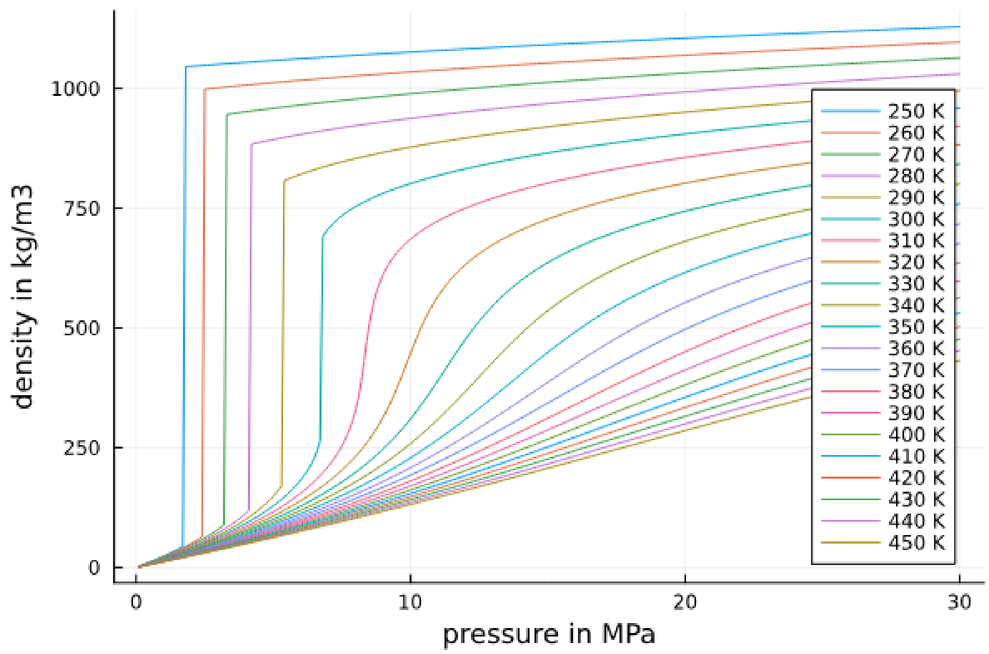

Figure 2.1: Plot of Span-Wagner pressure density isotherms. Julia code from [3] was used to reproduce the results in [5]. The vertical isotherm segments cover the binodal region, defined by equal fugacity along any isotherm.

In the $R^{-1} > 0$, $F \to \infty$ case (Section A.1.2), another analytic solution (A.4), (A.36) is found. An extra pipe-top condition, the strain rate, can be exchanged to determine a pipe-bottom condition, e.g., the pressure.

Specifically, we choose a pipe simulation that solves a PDE with conservation of mass A.2 and conservation of momentum A.42.

Variable	Value	Description
g (m s^{-2})	9.81	Gravitational acceleration
p_1(Pa)	6.8	Pressure at bottom of pipe
T_1(K)	301	Temperature at bottom of pipe
Z(m)	550	Max pipe depth
f(m^{-1})	.1	Friction factor
d(m)	.1	Pipe diameter
ρu(kg m^{-2} s^{-1})	400	Mass flux

Table 2.2: Summary of simulation parameter and boundary conditions used

2.2 Simple reservoir simulation

Now we discuss the reservoir simulation. The pipe model is then coupled with a model of 2D axisymmetric Darcy flow in a porous medium, also with mass and momentum conservation

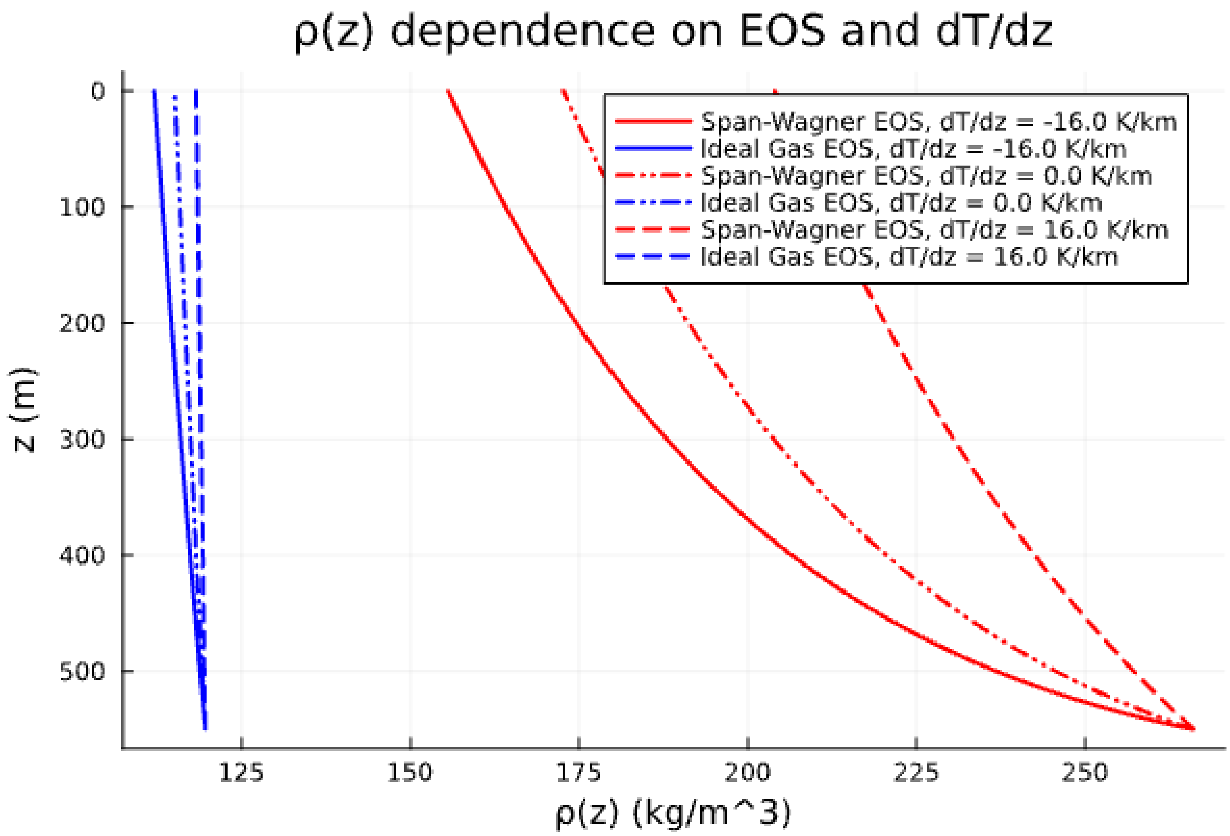

Figure 2.2: We compare the value of $\rho(z)$ down the pipe for different Γ_0 values using both Ideal Gas and Span-Wagner EoS.

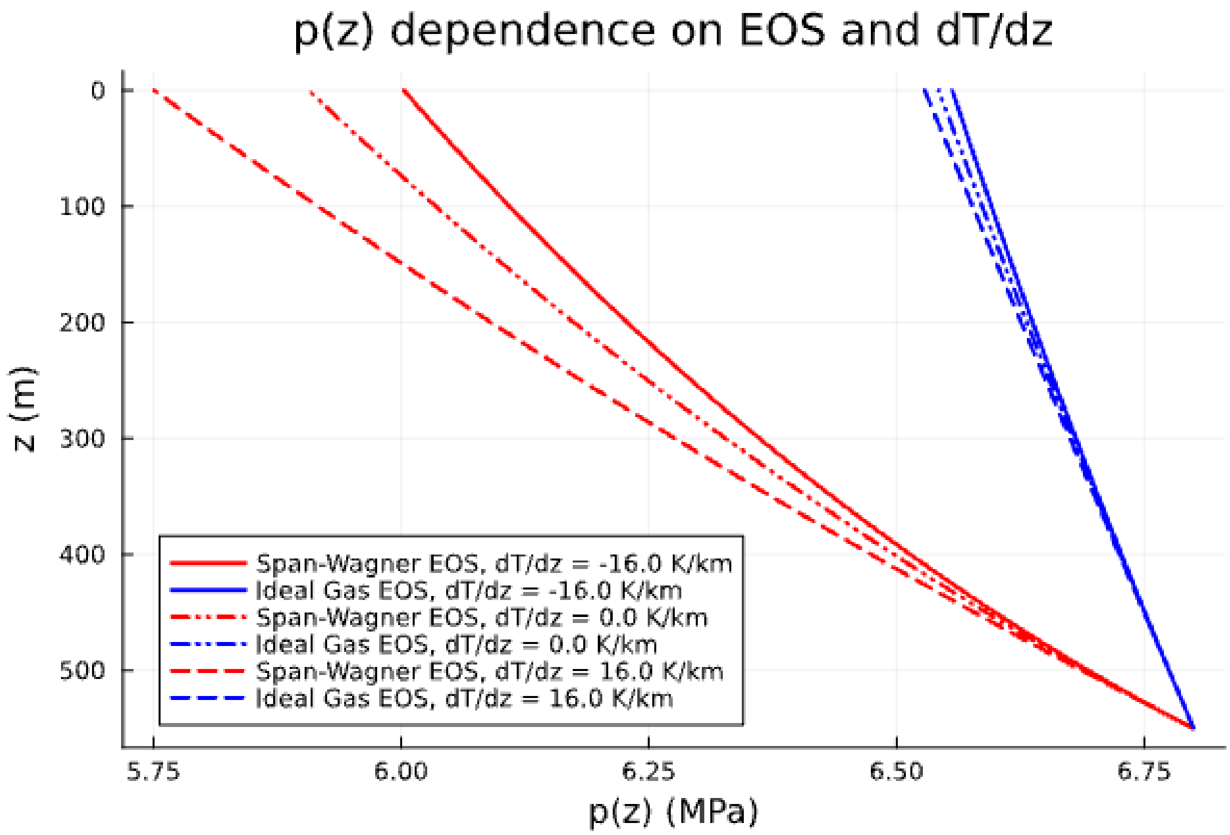

Figure 2.3: We compare the value of $p(z)$ down the pipe for different $\frac{dT}{dz}$ using both Ideal Gas and Span-Wagner EoS.

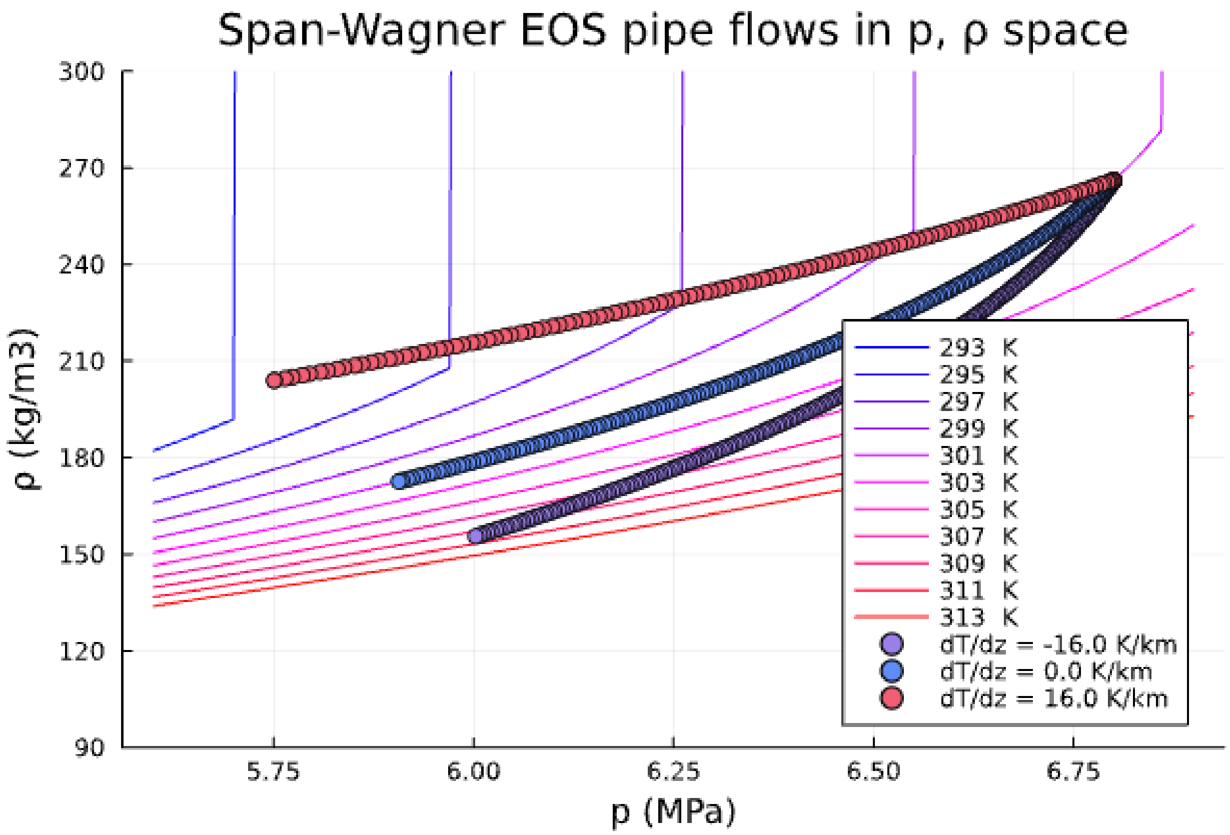

Figure 2.4: We look at the path down the pipe in p, ρ space for different $\frac{dT}{dz}$ values using Span-Wagner EoS. The colored lines are isotherms. We see the red curve of $\frac{dT}{dz} = 16K/km$ enters the binodal region, which means a phase change would occur with this temperature gradient under these conditions.

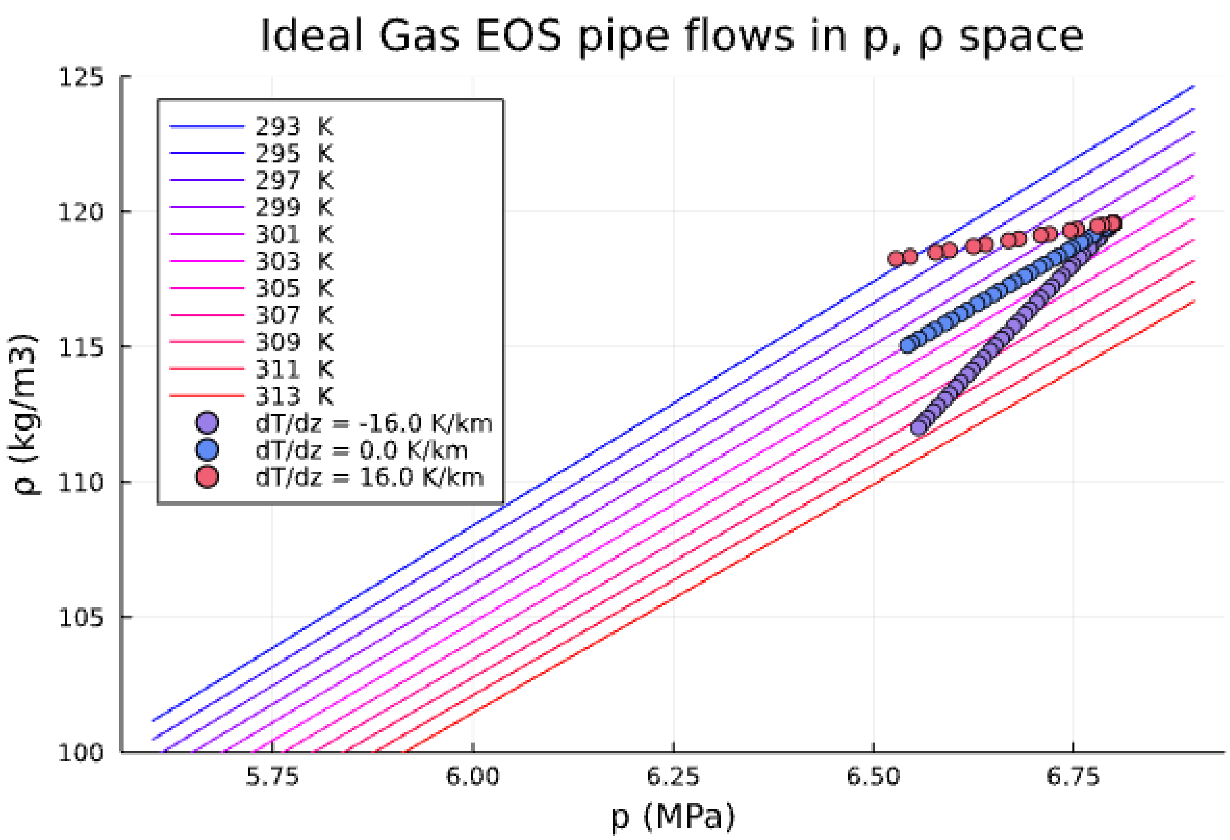

Figure 2.5: We look at the path down the pipe in p, ρ space for different dT/dz values using Ideal Gas EoS. The colored lines are isotherms. The p axis is the same as for 2.4 .

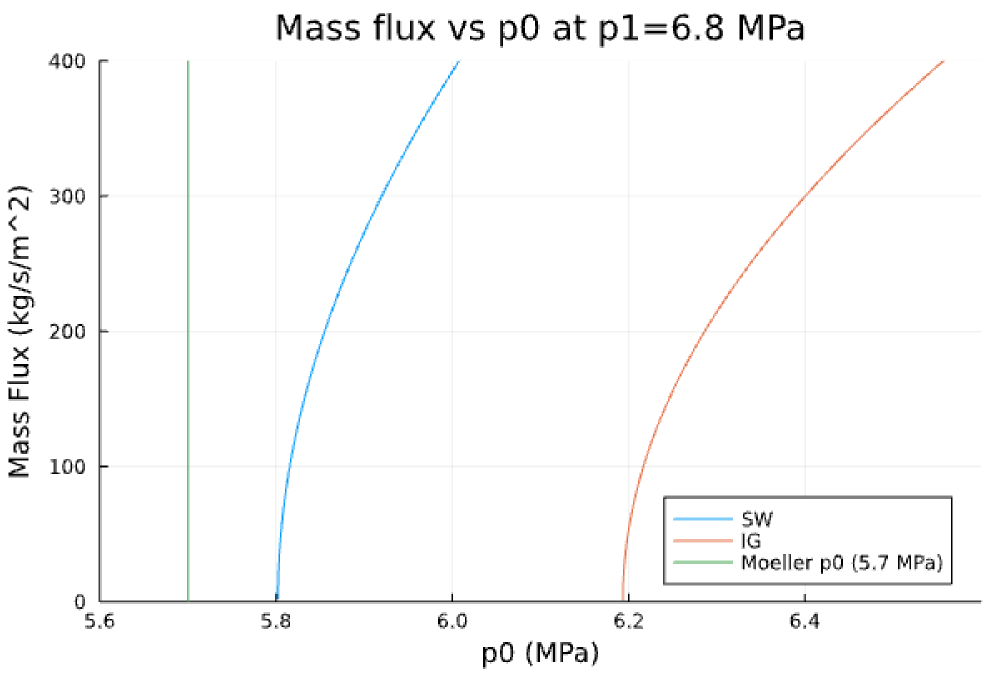

Figure 2.6: We compare the p_0 as a function of mass flux for a given p_1 in the pipe using Ideal Gas vs Span-Wagner EoS. We see that the minimum possible p_0 for Span-Wagner is much closer to the measured value in [2]. This drastic difference in even hydrostatic pressure (0 flux) means Span-Wagner EoS will predict flow for some rock p_∞ values when Ideal Gas EoS does not. Here we use a fixed $dT/dz = -16\text{K/km}$ and instead varies ρu to solve for p_0.

laws. This simulation is isothermic and includes energy conservation. The fluid is pumped out from a central pipe into a water-filled reservoir in the porous rock. Several experiments were run, changing the EoS for the fluid from Ideal Gas to the Span-Wagner [4] EoS, which is a more specific set of equations to more closely predict CO_2. The reservoir simulation's equations are explained in more detail on this webpage.

The reservoir simulation solves the PDEs in A.2.

2.3 Coupling

We propose the following very simple coupling between the 1D pipe simulation and the rock simulation 2.9. We identify $\rho u A$ and p_1 in the pipe and the rock. We find the point on the $\rho u A, p_1$ curve such that pipe and rock simulation intersect.

For the rock simulation, we are able to compute $p_1(t)$ given a flow rate and p_∞, which we can then use with the pipe simulation to compute $p_0(t)$. This matches physical reality, as p_∞ is derived from the properties of the reservoir, and the flow rate is what we have control over at the injection site using a compressor. Together, these two boundary values control the entire system.

We make the assumption that the time scale of the reservoir simulation is long enough relative to the pipe, which lets us assume that the pipe will achieve a steady state at each reservoir time step. This is how we create 2.8.

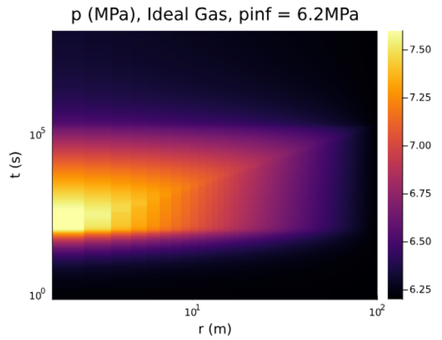

(a) Ideal Gas EOS – Pressure

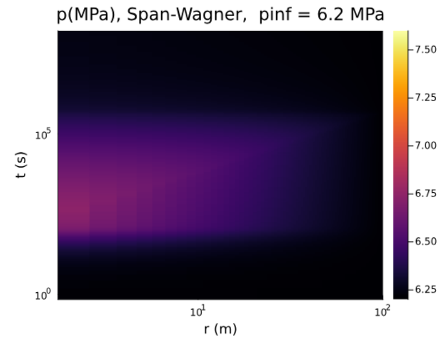

(b) Span-Wagner EOS – Pressure

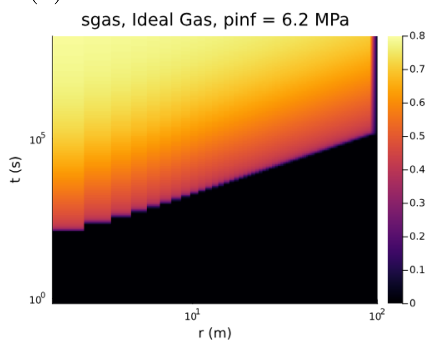

(c) Ideal Gas EOS – Gas Saturation

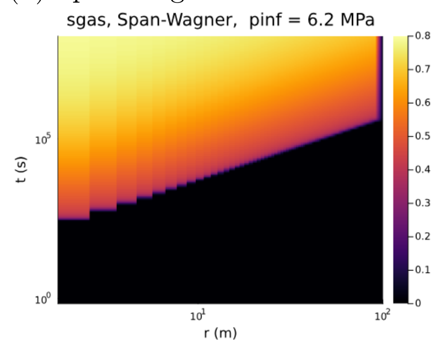

(d) Span-Wagner EOS – Gas Saturation

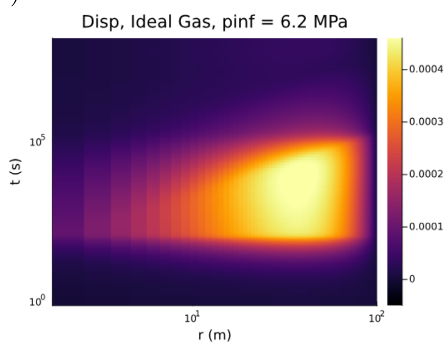

(e) Ideal Gas EOS – Displacement

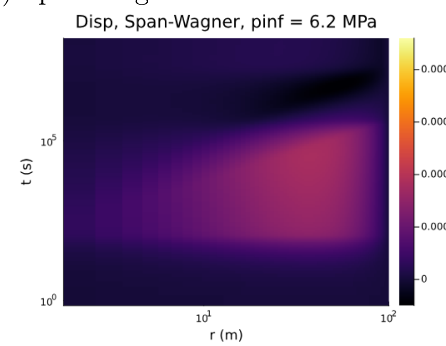

(f) Span-Wagner EOS – Displacement

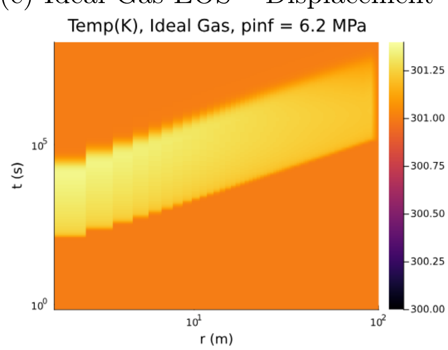

(g) Ideal Gas EOS – Temperature

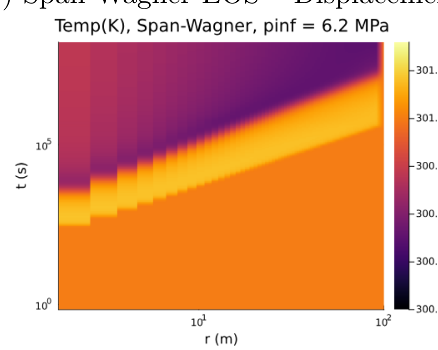

(h) Span-Wagner EOS – Temperature

Figure 2.7: Comparison of Ideal Gas and Span-Wagner EOS results for pressure, gas saturation, displacement, and temperature in the reservoir simulation with $p_\infty = 6.2\text{MPa}$ and mass flow $\rho u A = 13.76\text{kg/s}$. We note that pressure increase and displacement are around half for Span-Wagner than they are for Ideal Gas, which we attribute to the difference in density calculation.

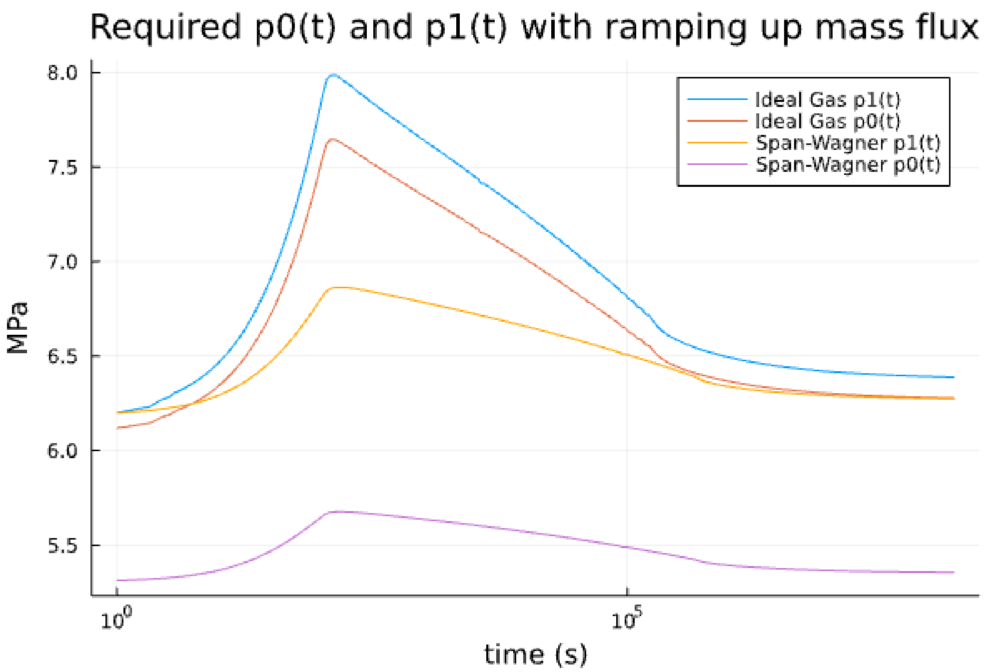

Figure 2.8: We compare the coupled $p_1(t)$ and $p_0(t)$ throughout the reservoir simulation between Ideal Gas and Span-Wagner EOS. We see the initial pressure spike for Ideal Gas is much higher than it is for Span-Wagner. The difference between p_0 and p_1 is much greater for Span-Wagner, due to the increased density for the same temperature and pressure. The initial increase before the dropoff is due to ramping up flowrate for the first 100 seconds, so that there is not an immediate shock to flow rate. During the first 100 seconds, the flow rate is $rate(t) = \min(1, t/100) * \rho u A$. The maximum flow rate, 13.76 kg/s was chosen, as any greater flow rate would raise the pressure into the binodal region, indicating liquefaction of the CO_2. In this plot, $p_\infty = p_1(0) = 6.2MPa$.

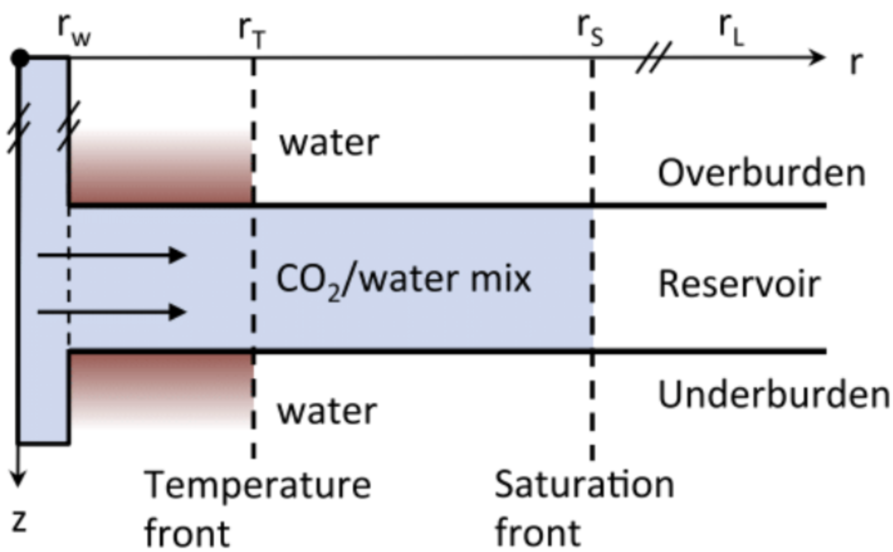

Figure 2.9: Schematic of pipe/rock coupling for CO_2 injection [1, their Fig. 1]. The area of the coupling for the pipe is πr_w^2 and the area for the Rock is $2\pi r_w d$, where d is the height of the overburden minus the height of the underburden. Since we want total flow to be seamless, we get $u|_{r=r_w} = \frac{r_w}{2d} u|_{z=Z}$ as the appropriate flow per area. That is to say, the total horizontal flow into the rock formation is exactly equal to the total vertical flow in the pipe, adjusted only for the difference in area.

Chapter 3

Results and Discussion

3.1 Computational Performance

The computational cost of each equation of state is evaluated based on pipe and reservoir simulation experiments run on a 2021 14-inch M1 Macbook Pro.

Tables 3.1 and 3.2 summarize the performance comparison.

Metric	**Ideal Gas Law**	**Span-Wagner EOS**
Computation time (s)	0.0356	5.417
Memory usage (MB)	16.19	2684

Table 3.1: Comparison of computational cost between the two EOS models in the pipe simulation. Span-Wagner is much slower and uses much more memory due to the added complexity of the EOS.

Metric	**Ideal Gas Law**	**Span-Wagner EOS**
Computation time (s)	50.14	862.72
Memory usage (MB)	155	66

Table 3.2: Comparison of computational cost between the two EOS models in the reservoir. The memory usage for Span-Wagner is less than for Ideal Gas, but the Span-Wagner simulation takes an order of magnitude longer.

3.2 Pressure and Density Distribution in Pipe

Figure 2.3 shows $p(z)$ down the pipe. Given the same p_1 at the bottom of the pipe, the required p_0 at the top of the pipe is considerably lower for Span-Wagner than it is for Ideal Gas. Additionally the temperature gradient impacts the Span-Wagner calculation for pressure more as well.

This pressure difference is explained by Figure 2.2, as the density down the pipe for Span-Wagner is at points double the density for Ideal Gas. This greater density impacts the pressure, so the weight of the column is underpredicted by the Ideal Gas EOS.

Figure 2.6 shows the impact of wellhead pressure p_0 on mass flux given a constant p_1. We see that we can inject at the same speeds for lower pressure. Additionally, the Span-Wagner borehole pressure is much closer to the measured value found in [2].

3.3 Pressure Distribution in Reservoir

Figure 2.8 shows the pressure distribution at the linkage point for the two equations of state, as well as the required injection pressure in order to maintain the ramping up mass flux. Since the Ideal Gas Law underestimates density, it leads to a lower pressure gradient between $p_0(t)$ and $p_1(t)$. In the reservoir however, this lower density causes a greater increase in pressure with respect to time, as the Ideal Gas pressure peak is higher than the Span-Wagner pressure peak. This can also be attributed to the difference in density, as Darcy's law states the volumetric flux $u \propto \nabla p$. These different EOS simulations have the same ramping up mass flux ρu function. This explains the fact that the Ideal Gas simulation, which predicts lower density and thus higher mass flow, has a higher pressure increase than the Span-Wagner simulation. Together, this means the Ideal Gas EOS underestimates the pressure gradient in the pipe and overestimates the pressure increase in the reservoir.

Figure 2.7 shows that the pressure distribution difference from the different density calculations and volumetric flow rates leads to a difference in rock displacement as well, as effective strength in the rock is also lessened for Span-Wagner.

3.4 Phase change detection

The peak of the orange curve in Figure 2.8 occurs at a pressure right below the vertical isotherm for $301K$ as shown in Figure 2.1. The coupled simulations allow us to compute the flow for CO_2 as long as it remains in the gaseous regime of the phase diagram, i.e. below the binodal curve. This then allows us to predict the maximum flow rate before the pressure rise passes the binodal curve and liquefaction would occur.

In the pipe simulation, Figure 2.4 demonstrates that a negative or 0 temperature gradient remains below the binodal curve, but the red curve with $dT/dz = 16.0K/km$ enters the binodal curve, so we can predict a phase change in this region.

If we look instead for the ideal gas curves in Figure 2.5, we see no phase change region is present and thus the Ideal Gas EOS cannot predict phase changes.

Chapter 4

Conclusion and Future Work

4.1 Conclusion

This thesis investigates the impact of using two different equations of state, Ideal Gas Law and Span-Wagner EOS, on modeling CO_2 flow in a pipe and porous medium. Using the coupled computational simulations, we analyze how the choice of EOS affects pressure and density.

Our key finding is that in the conditions relevant for pipe flow, the Ideal Gas Law underestimates the pressure differential from the weight of the column, due to having a much lower value for density than Span-Wagner does. It also overpredicts the pressure increase with time in the reservoir. In order to achieve the same mass flow, using the Ideal Gas EOS would overpredict the required wellhead and bottom of pipe pressures, and underestimate the achievable injection rate. Using the more realistic Span-Wagner EOS predicts a lower required wellhead pressure as well as lower pore pressure and displacements in the porous reservoir. This means that operators can inject faster, more safely, and with lower seismic risk if they use models with the more realistic EOS.

Overall, the results demonstrate that choosing the appropriate EOS is critical for accurate modeling of CO_2 flow in porous media, particularly in applications like carbon capture and storage (CCS) where high pressures are common.

4.2 Future Work

We propose several extensions of this study:

4.3 Modeling Other Reservoir Conditions

Although this simulation is currently based on physical parameters in [2], it was developed with the ability to be adapted to other conditions to reproduce new results.

4.3.1 Transient Flow Simulations

The pipe flow simulation focuses on steady-state condition whereas the reservoir simulation modeled transient flow. We propose incorporating time dependence into the pipe simulation to match the transient reservoir model, enabling a more realistic representation of coupled dynamics and the potential for gas cooling due to expansion.

4.3.2 Coupled Thermal Effects

We have a very basic model for temperature variations in this study. Including energy equations would allow us to better predict density evolution by accounting for thermodynamic energy conservation, rather than assuming linear gradients and isothermicity. We would include energy balance, including the correct terms accounting for the EOS. Additionally, we would like to implement heat transfer with the formation by means of a Newton ΔT model with a calibrated heat conductivity.

4.3.3 Phase Change Handling

Currently we are only able to detect the conditions of phase change. We could extend to being able to implement the liquefaction and evaporation processes in the binodal zone, allowing both liquid and gaseous CO_2.

4.3.4 Turbulence in the Pipe

The pipe simulation is approximated as one-dimensional, whereas it could be more accurately modeled with 3D cylindrical geometry and more accurate turbulence models.

4.3.5 Capillary Pressure in the Reservoir

We have made the assumption that there is no capillary pressure in the reservoir. The impact of modifying this parameter would be worth studying.

4.4 Final Remarks

This thesis provides a computational framework for modeling coupled CO_2 flow in a pipe along with a porous medium while comparing different equations of state. The results highlight the trade-offs between accuracy and computational cost, offering valuable insights for future modeling efforts in geologic storage, enhanced oil recovery, and other subsurface engineering applications.

Appendix A

APPENDICES

A.1 Steady state

Details are included here for reproducibility. To obtain a first-order system, define a longitudinal expansion rate

$$\dot{\varepsilon} = \frac{du}{dz} \in \mathbb{R} \tag{A.1}$$

[6, Art. 11 Eq. 6]. Then the 1D, steady conservation laws for mass (density $\rho > 0$) and vertical momentum (density $\rho u \in \mathbb{R}$) are

$$\frac{d}{dz}(\rho u) = 0, \tag{A.2}$$

$$\frac{d}{dz}\left(\rho u^2 + p(T,\rho) - \mu\dot{\varepsilon}\right) = g\rho \tag{A.3}$$

[6, Eqs. 1.1, 11.8a–b], where: $p(\cdot,\cdot) > 0$ is a known Equation-of-State pressure function from ρ and temperature $T > 0$; $\mu > 0$ is $\frac{4}{3}\cdot$ uniform dynamic viscosity;[1] and $g > 0$ is uniform gravity acceleration from the pipe top $z = 0$ toward the pipe bottom $z = Z > 0$. Equation A.2 implies

$$\rho = \rho_0/\alpha \qquad (\text{if } u_0 \neq 0) \tag{A.4}$$

[6, Eq. 11.9], where

$$\alpha = u/u_0 > 0. \tag{A.5}$$

That is, for all $0 < z \leq Z$, u will retain the sign of

$$u_0 = u\big|_{z=0} \in \mathbb{R}. \tag{A.6}$$

A.1.1 Inviscid case, $\mu = 0$

Equations A.3, A.4 imply

$$\frac{d}{dz}\left(u + \frac{1}{\rho_0 u_0} p\left(T, \frac{\rho_0 u_0}{u}\right)\right) = \frac{g}{u}. \tag{A.7}$$

[1] The $\frac{4}{3}$ factor arises from geometric considerations [6, Art. 11.1].

For an ideal gas

$$p(T, \rho) = R_s T \rho, \tag{A.8}$$

where $R_s > 0$ is the specific gas constant. Then (A.7) becomes

$$g = u \frac{d}{dz} \left(u + \frac{R_s T}{u} \right) \tag{A.9}$$

$$= \left(u - \frac{R_s T}{u} \right) \frac{du}{dz} + R_s \Gamma, \tag{A.10}$$

where the temperature gradient is

$$\Gamma = \frac{dT}{dz} \in \mathbb{R}. \tag{A.11}$$

Introducing the pipe-top Froude number

$$F = \frac{|u_0|}{\sqrt{gZ}} > 0 \tag{A.12}$$

and pipe-top Mach number

$$0 < M = \frac{|u_0|}{\sqrt{R_s T_0}} \ll 1, \tag{A.13}$$

(A.5), (A.10) imply

$$\frac{1}{F^2} = \left(\alpha - \frac{1}{M^2 \alpha} \right) Z \frac{d\alpha}{dz} + \frac{R_s Z}{u_0^2} \Gamma. \tag{A.14}$$

We can consider either instant equilibration with the formation,

$$T = T_0 + \Gamma_0 z \tag{A.15}$$

or an isothermal case

$$T = T_0. \tag{A.16}$$

In either case, the implicit solution of (A.14), (A.16) is

$$\left(\frac{1}{F^2} - \frac{1}{G^2} \right) \frac{2z}{Z} = \alpha^2 - 1 - \frac{1}{M^2} \ln \alpha^2 \tag{A.17}$$

$$= 2 \left(\frac{1}{M^2} - 1 \right) (1 - \alpha) + \left(\frac{1}{M^2} + 1 \right) (1 - \alpha)^2 + \frac{2}{M^2} \sum_{n=3}^{\infty} \frac{1}{n} (1 - \alpha)^n, \tag{A.18}$$

where

$$G = \frac{|u_0|}{\sqrt{R_s \Gamma_0 Z}} \tag{A.19}$$

is a new dimensionless number. Equation A.17 is plotted in Fig. A.1 for $\Gamma_0 = 0$. Equations (A.5), (A.12), (A.14), (A.16), (A.19) and $g > R_s \Gamma_0$ imply that for $0 < \alpha < M^{-1}$, α is monotonically decreasing as z increases.

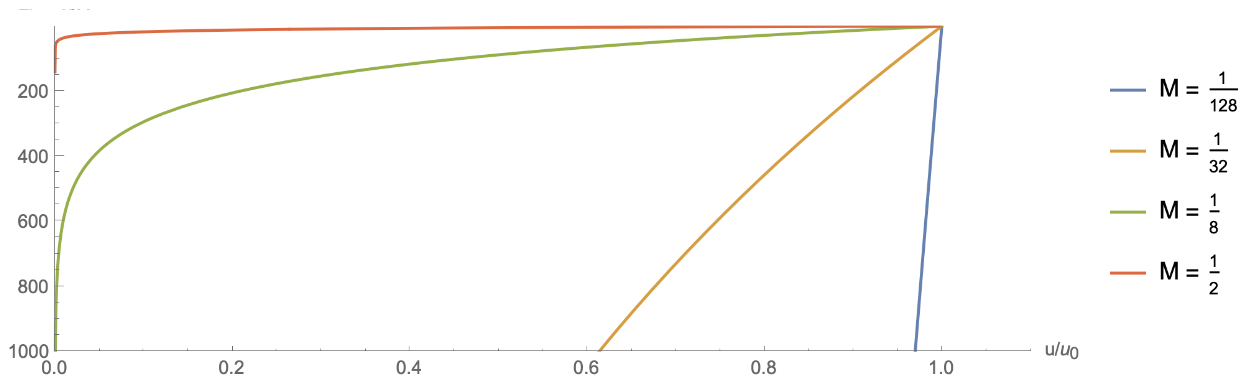

Figure A.1: Plots of u/u_0 (abscissa) vs $2F^{-2}z/Z$ (ordinate) from the inviscid, $g > 0$ case, Eqs. A.12, A.17, for various M (A.13) as indicated. Physically, by Eq. A.4, the u/u_0 decrease reflects the ρ increase toward the pipe bottom.

A.1.2 Viscous case $\mu > 0$

Equations A.2, A.3, A.4 imply that the first-order system can be written as (A.1) and[2]

$$\mu \frac{d\dot{\varepsilon}}{dz} = \left(\rho_0 u_0 \left(\left(1 - \frac{1}{u^2} \frac{\partial p}{\partial \rho} \right) \dot{\varepsilon} - \frac{g}{u} \right) + \frac{\partial p}{\partial T} \Gamma \right)_{p \to p(T, \rho_0 u_0/u)} . \tag{A.20}$$

Equations A.4, A.8, A.20 imply

$$\frac{\mu}{\rho_0 u_0} \frac{d\dot{\varepsilon}}{dz} = \left(1 - \frac{R_\mathrm{s} T}{u^2} \right) \dot{\varepsilon} + \frac{1}{u} \left(R_\mathrm{s} \Gamma - g \right) . \tag{A.21}$$

By (A.1), (A.16), (A.21), neglecting $g \to 0$,

$$\frac{\mu}{\rho_0 u_0} \frac{d\dot{\varepsilon}}{dz} = \left(1 - \frac{R_\mathrm{s} T_0}{u^2} \right) \frac{du}{dz} \tag{A.22}$$

$$= \frac{d}{dz} \left(u + \frac{R_\mathrm{s} T_0}{u} \right) \tag{A.23}$$

$$\Rightarrow \quad \frac{Z}{R u_0} \dot{\varepsilon} - \frac{A}{R} = (\alpha - 1) \left(\alpha - \frac{1}{M^2} \right) \frac{1}{\alpha}, \tag{A.24}$$

where the absolute value of

$$R = \frac{\rho_0 u_0 Z}{\mu} = \frac{\rho_0 u_0^2}{\mu \dot{\varepsilon}_0} A \in \mathbb{R} \tag{A.25}$$

is the pipe-top Reynolds number, and

$$A = \frac{Z \dot{\varepsilon}_0}{u_0} = -Z \frac{d \ln \rho}{dz} \bigg|_{z=0} \in \mathbb{R} \tag{A.26}$$

[2] Check if $\mu \to \infty$ then a solver should get $\dot{\varepsilon} = \dot{\varepsilon}_0 \Rightarrow u = u_0 + \dot{\varepsilon}_0 z$.

(by Eqs. A.1, A.2) is the pipe-top Atwood number. Below we will see that A can be tuned e.g., to achieve an $z = Z$ boundary condition. Therefore where $\dot{\varepsilon} \neq 0$, Eqs. A.24, A.25 imply[3]

$$\frac{Ru_0}{Z}\frac{1}{\dot{\varepsilon}} = \alpha \big/ \left(M^{-2} - \left(1 + M^{-2} - A/R\right)\alpha + \alpha^2\right) \tag{A.27}$$

$$\Rightarrow \quad \frac{R}{Z}\frac{dz}{d\alpha} = \frac{1}{\alpha_+ - \alpha_-}\left(\frac{\alpha_+}{\alpha - \alpha_+} - \frac{\alpha_-}{\alpha - \alpha_-}\right) \tag{A.28}$$

$$= \frac{R}{A} + \frac{1}{\alpha_+ - \alpha_-}\sum_{n=1}^{\infty}\left(\frac{\alpha_-}{(\alpha_- - 1)^{n+1}} - \frac{\alpha_+}{(\alpha_+ - 1)^{n+1}}\right)(\alpha - 1)^n\,, \tag{A.29}$$

where the (A.27) denominator roots

$$\alpha_\pm = \frac{1 + M^{-2} - A/R}{2}\left(1 \pm \sqrt{1 - \frac{4M^{-2}}{\left(1 + M^{-2} - A/R\right)^2}}\right) \tag{A.30}$$

$$= \begin{cases} M^{-2} - \frac{A}{R}\left(1 + M^2\right) \\ 1 + \frac{A}{R}M^2 \end{cases} + O(M^4). \tag{A.31}$$

Note that Eq. A.28 is positive for $\alpha > \alpha_+$ and $0 < \alpha < \alpha_-$, and negative otherwise. By (A.30), both $\alpha_\pm$ are real (or compose a complex-conjugate pair) if R/A is not (or is) in the typically small interval

$$0 < \left(M^{-1} + 1\right)^{-2} < R/A < \left(M^{-1} - 1\right)^{-2} = \left(M^{-1} + 1\right)^{-2} + O(M^3). \tag{A.32}$$

By (A.13), (A.31), typically

$$M^{-2}\big/\,\alpha_- = \alpha_+ \gg \alpha_- > 0. \tag{A.33}$$

Also, we can view $u_\pm$ as the primary parameters and obtain

$$M = 1\big/\sqrt{\alpha_+\alpha_-}\,, \tag{A.34}$$

$$A/R = \left(\alpha_+ - 1\right)\left(\alpha_- - 1\right). \tag{A.35}$$

Therefore Eq. A.28 implies the inverse solution

$$R\frac{z}{Z} = \frac{1}{\alpha_+ - \alpha_-}\left(\alpha_+ \ln\left|1 - \frac{\alpha - 1}{\alpha_+ - 1}\right| - \alpha_- \ln\left|1 - \frac{\alpha - 1}{\alpha_- - 1}\right|\right) \tag{A.36}$$

$$= \frac{1}{\alpha_+ - \alpha_-}\sum_{n=1}^{\infty}\left(\frac{\alpha_-}{(\alpha_- - 1)^n} - \frac{\alpha_+}{(\alpha_+ - 1)^n}\right)\frac{(\alpha - 1)^n}{n} \tag{A.37}$$

$$= \frac{R}{A}(\alpha - 1) + \frac{M^{-2} - 1}{2}\frac{R^2}{A^2}(\alpha - 1)^2 + O\left((\alpha - 1)^3\right). \tag{A.38}$$

Given M, $R\,\mathrm{sgn}\,u_0$ and u_1 or p_1, to fulfill a boundary condition such as

$$\alpha|_{z=Z} = \alpha_1 \quad \text{or} \tag{A.39}$$

$$p|_{z=Z} = p_1 = M^{-2}\rho_0 u_0^2\big/\,\alpha_1 \tag{A.40}$$

[3]The purpose of (A.29) is to illuminate the dz/du behavior near $u = u_0$.

(by Eqs. A.4, A.8, A.13), solve

$$R = \frac{1}{\alpha_+ - \alpha_-}\left(\alpha_+ \ln\left|1 - \frac{\alpha_1 - 1}{\alpha_+ - 1}\right| - \alpha_- \ln\left|1 - \frac{\alpha_1 - 1}{\alpha_- - 1}\right|\right) \tag{A.41}$$

and (A.30) simultaneously for A/R.

A.1.3 Darcy–Weisbach alternative to viscous drag

Replace (A.3) by

$$\frac{d}{dz}\left(\rho u^2 + p(T,\rho)\right) = g\rho - f\rho u^2 \tag{A.42}$$

$$\Rightarrow \quad \left(1 - \frac{\partial p}{\partial \rho}\frac{1}{u^2}\right)\frac{du}{dz} = \frac{g}{u} - fu - \frac{1}{\rho_0 u_0}\frac{\partial p}{\partial T}\mathit{\Gamma} \quad \text{(by Eqs. A.4, A.11, } u_0 \neq 0\text{)} \tag{A.43}$$

$$\Rightarrow \quad \left(1 - \frac{R_\mathrm{s} T}{u^2}\right)\frac{du}{dz} = \frac{g - R_\mathrm{s}\mathit{\Gamma}}{u} - fu \qquad \text{(by Eq. A.8)} \tag{A.44}$$

$$\Rightarrow \quad \left(1 - \frac{R_\mathrm{s}}{u^2}\left(T_0 + \mathit{\Gamma}_0 z\right)\right)\frac{du}{dz} = \frac{g - R_\mathrm{s}\mathit{\Gamma}_0}{u} - fu \qquad \text{(by Eq. A.15)} \tag{A.45}$$

$$\Rightarrow \quad \left(1 - \frac{1}{\alpha^2}\left(M^{-2} + G^{-2}\frac{z}{Z}\right)\right) Z\frac{d\alpha}{dz} = \frac{F^{-2} - G^{-2}}{\alpha} - fZ\alpha, \quad \text{(by Eqs. A.5, A.12, A.13, A.19)} \tag{A.46}$$

where

$$f = \frac{1}{2}\frac{\text{Darcy friction factor}}{\text{hydraulic diameter}}. \tag{A.47}$$

In terms of reduced density and inverse-temperature $\delta = \rho/\rho_\mathrm{c} > 0$ and $\tau = T_\mathrm{c}/T > 0$, the dimensionless form of (A.43) is

$$\left.\left(\left(1 - \frac{\partial p}{\partial \delta}\frac{1}{\rho_\mathrm{c} u_0^2 \alpha^2}\right) Z\frac{d\alpha}{dz} + \frac{Z}{\rho_0 u_0^2}\frac{\partial p}{\partial \tau}\frac{d\tau}{dz}\right)\right|_{\substack{\delta \to \rho_0/\rho_\mathrm{c}\alpha \\ \tau \to T_\mathrm{c}/(T_0 + \mathit{\Gamma}_0 z)}} = \frac{F^{-2}}{\alpha} - fZ\alpha. \tag{A.48}$$

We may define a background state $\bar{u} = 0$, $\bar{\rho}$ that trivially conserves mass, so that (A.15), (A.42) imply a hydrostatic balance

$$g\bar{\rho} = \left.\left(\frac{\partial p}{\partial \rho}\frac{d\bar{\rho}}{dz} + \frac{\partial p}{\partial T}\mathit{\Gamma}_0\right)\right|_{\substack{T \to T_0 + \mathit{\Gamma}_0 z \\ \rho \to \bar{\rho}}} \tag{A.49}$$

$$\Rightarrow \quad \frac{g}{R_\mathrm{s}\mathit{\Gamma}_0} = T\left.\frac{d\ln\bar{\rho}}{dT}\right|_{T \to T_0 + \mathit{\Gamma}_0 z} + 1 \qquad \text{(by Eq. A.8)} \tag{A.50}$$

$$\Rightarrow \quad \bar{\rho} = \bar{\rho}_0 \left.\left(T/T_0\right)^{\frac{g}{R_\mathrm{s}\mathit{\Gamma}_0} - 1}\right|_{T \to T_0 + \mathit{\Gamma}_0 z}. \tag{A.51}$$

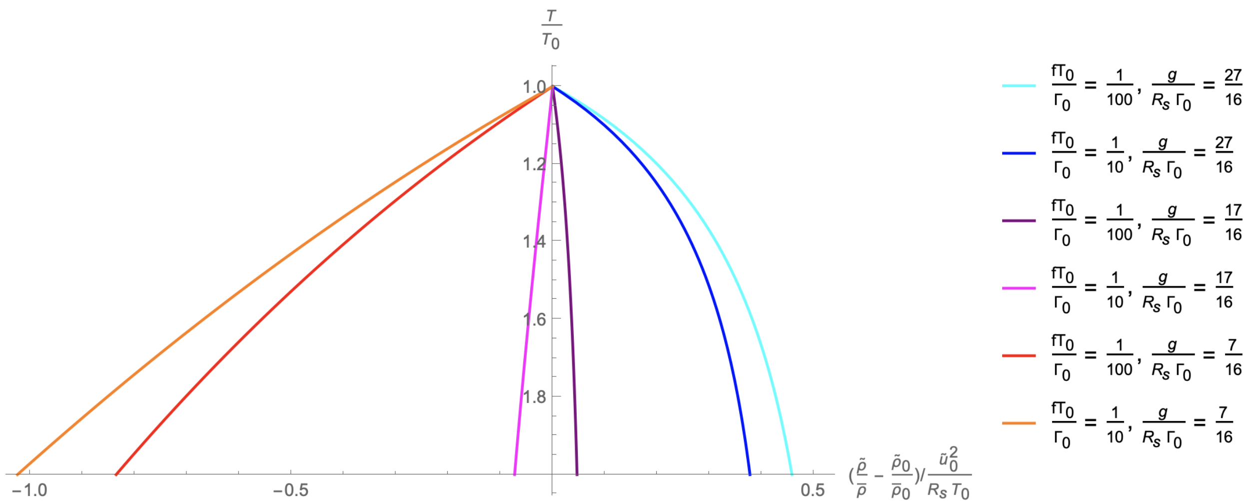

Figure A.2: Density perturbation $\widetilde{\rho}$ (abscissa, Eq. A.55 with $\epsilon \to 0$) relative to hydrostatic density $\bar{\rho}$ (A.51), pipe-top values (subscripts 0) and perturbation Mach number $\frac{\widetilde{u}_0^2}{2R_\mathrm{s}T_0} \ll 1$; vs relative temperature (ordinate). Curve colors show ambient vertical temperature-gradient $\mathit{\Gamma}_0$ (A.15) relative to $fT_0 \propto$ Darcy-Weisbach friction, and to $g/R_\mathrm{s} \propto$ gravity. Note how $\mathit{\Gamma}_0$ affects even the simplest density perturbation behavior, even for an ideal gas.

A perturbation[4] $\epsilon\widetilde{u}$, $\epsilon^2\widetilde{\rho}$ to $\bar{u}$, $\bar{\rho}$ is given by

$$\widetilde{u} - \frac{\widetilde{u}_0\bar{\rho}_0}{\bar{\rho}} = O\left(\epsilon^2\right), \tag{A.52}$$

$$\left(\frac{\partial p}{\partial \rho}\frac{d}{dz} + \frac{\partial^2 p}{\partial \rho^2}\frac{d\bar{\rho}}{dz} + \frac{\partial^2 p}{\partial T \partial \rho}\mathit{\Gamma}_0 - g\right)\Bigg|_{\substack{T \to T_0 + \mathit{\Gamma}_0 z \\ \rho \to \bar{\rho}}} \widetilde{\rho} + \left(f\bar{\rho} - \frac{d\bar{\rho}}{dz}\right)\widetilde{u}^2 = O\left(\epsilon^2\right) \tag{A.53}$$

$$\Rightarrow \quad \left(T\frac{d}{dT}\frac{\widetilde{\rho}}{\bar{\rho}} + \frac{\widetilde{u}_0^2}{R_\mathrm{s}}\left(\frac{f}{\mathit{\Gamma}_0} + \frac{1}{2}\frac{d}{dT}\right)\frac{\bar{\rho}_0^2}{\bar{\rho}^2}\right)\Bigg|_{T \to T_0 + \mathit{\Gamma}_0 z} = O\left(\epsilon^2\right) \quad \text{(by Eq. A.8).} \tag{A.54}$$

Therefore by (A.15), (A.51)

$$\frac{\widetilde{\rho}}{\bar{\rho}} - \frac{\widetilde{\rho}_0}{\bar{\rho}_0} + \frac{\widetilde{u}_0^2}{2R_\mathrm{s}T_0}\left(\frac{\gamma+1}{\gamma}\left(\left(\frac{T}{T_0}\right)^{\gamma} - 1\right) + \frac{2fT_0}{(\gamma+1)\mathit{\Gamma}_0}\left(\left(\frac{T}{T_0}\right)^{\gamma+1} - 1\right)\right) = O\left(\epsilon^2\right) \tag{A.55}$$

(Fig. A.2), where $\gamma = 1 - 2g/R_\mathrm{s}\mathit{\Gamma}_0$.

[4]The distinguished perturbation scaling reflects that (A.42) has no term linear in u.

A.1.4 Permuted Equation of State

In Eqs. A.4 and A.42 (or another Momentum Eq.), one could make p the primary variable instead of ρ:

$$\begin{aligned}\rho(p,T)u &= \rho(p_0,T_0)u_0 && \text{(A.56)}\\ &=: \rho_0 u_0 \qquad \text{(if } u_0 \neq 0\text{)}, && \text{(A.57)}\\ \frac{d}{dz}\left(u+\frac{p}{\rho_0 u_0}\right) &= \frac{g}{u} - fu. && \text{(A.58)}\end{aligned}$$

Then one could solve for u_0 in terms of $p_1 := p(Z)$. To get u from (A.56) or ρ_0 from (A.57) requires p_0 to be above the spinodal curve[1] $\rho \mapsto p$ defined by $(\partial\rho/\partial p)_T \to \infty$.

A.1.5 Steady conservation of energy

Conservation of specific energy may be expressed as

$$u\frac{d}{dz}\left(\frac{u^2}{2} - gz + cT\right) + \frac{1}{\rho}\frac{d}{dz}\left(\left(p(T,\rho) - \mu\dot{\varepsilon}\right)u - \kappa\mathit{\Gamma}\right) = 0 \tag{A.59}$$

[6, Eqs. 2.6, 11.8c], where c is isochoric specific heat capacity and κ is thermal conductivity. Applying (A.2) to (A.59) yields the first integral

$$\begin{aligned}\mathit{\Gamma} - \mathit{\Gamma}_0 &= \frac{u}{\kappa}\left(p\left(T,\rho\right) - \mu\dot{\varepsilon} + \rho\left(\frac{u^2}{2} - gz + cT\right)\right)\Bigg|_0^z && \text{(A.60)}\\ &\xrightarrow{(A.4)} \frac{u}{\kappa}\left(p\left(T,\frac{\rho_0 u_0}{u}\right) + \frac{\rho_0 u_0}{u}\left(\frac{u^2}{2} - gz + cT\right) - \mu\dot{\varepsilon}\right)\Bigg|_0^z && \text{(A.61)}\\ &\xrightarrow{(A.8)} \frac{\rho_0 u_0}{\kappa}\left((R_\mathrm{s}+c)T + \frac{u^2}{2} - gz - \frac{\mu}{\rho_0 u_0}u\dot{\varepsilon}\right)\Bigg|_0^z, && \text{(A.62)}\end{aligned}$$

where by Mayer's Relation, $R_\mathrm{s} + c$ is the isobaric specific heat capacity. Applying (A.1), (A.5), (A.11), (A.12), (A.15), (A.25), (A.26) to this would imply

$$\begin{aligned}\frac{1}{2} - \frac{A}{R} &= \frac{\alpha^2}{2} + H\frac{z}{Z} - \frac{Z}{R}\alpha\frac{d\alpha}{dz} && \text{(A.63)}\\ \Rightarrow \quad \alpha &= \sqrt{1 - 2\frac{A}{R} - 2H\left(\frac{z}{Z} + \frac{1}{R}\right) + 2\left(\frac{A}{R} + H\frac{Z}{R}\right)e^{Rz/Z}} && \text{(A.64)}\end{aligned}$$

that seems incompatible with either (A.17) as $|R| \to \infty$ or (A.36) as $F \to \infty$, where $H := \frac{(R_\mathrm{s}+c)\mathit{\Gamma}_0 Z}{u_0^2} - F^{-2}$ is another dimensionless number. If it is incompatible then it seems (A.15) and (A.59) are incompatible i.e., either $\mathit{\Gamma}$ must vary to conserve energy, or work must be done to maintain (A.16).

A.1.6 Flow Acceleration with Span–Wagner EoS

We start from the one-dimensional steady momentum equation including gravity and Darcy friction, in A.42 and A.43. This shows the sign of $\frac{du}{dz}$ with respect to the other variables as in A.44. We recalculate in the Span-Wagner case:

Generalization for Span–Wagner Equation of State

The Span–Wagner EoS is given by:

$$p(T,\rho) = \rho R_s T \left(1 + \delta \phi^r_\delta\right), \tag{A.65}$$

where:

$$\delta = \frac{\rho}{\rho_c}, \quad \tau = \frac{T_c}{T}, \quad \phi^r_\delta = \frac{\partial \phi^r}{\partial \delta}.$$

The required thermodynamic derivatives are:

Pressure derivative with respect to ρ:

$$\frac{\partial p}{\partial \rho} = R_s T \left(1 + 2\delta \phi^r_\delta + \delta^2 \phi^r_{\delta\delta}\right). \tag{A.66}$$

Pressure derivative with respect to T:

$$\frac{\partial p}{\partial T} = \rho R_s \left(1 + \delta \phi^r_\delta - \delta\tau \phi^r_{\delta\tau}\right). \tag{A.67}$$

Final Generalized Acceleration Equation

Substituting Eqs. (A.66) and (A.67) into Eq.A.43, we obtain:

$$\left(u - \frac{1}{u} R_s T \left(1 + 2\delta\phi^r_\delta + \delta^2 \phi^r_{\delta\delta}\right)\right) \frac{du}{dz} = g - fu^2 - R_s \Gamma_0 \left(1 + \delta\phi^r_\delta - \delta\tau\phi^r_{\delta\tau}\right). \tag{A.68}$$

We can then get that the sign of $\frac{du}{dz}$ will be the sign of $\frac{g - fu^2 - R_s T_0 (1 + \delta\phi^r_\delta - \delta\tau\phi^r_{\delta\tau})}{u - \frac{1}{u} R_s T \left(1 + 2\delta\phi^r_\delta + \delta^2\phi^r_{\delta\delta}\right)}$

We note that without the residual terms, this would be the same equation as the ideal gas case A.44.

A.1.7 Span-Wagner Phase Change Detection

The vertical ρ vs p isotherms in Figure 2.1 come from inversely computing $\rho(p,T)$, assuming equal fugacity.[5] However, the fluid can exist as either a single metastable phase (superheated liquid or supersaturated gas) or as a stable two-phase mixture of liquid and gas. The actual state depends on the history of the system and whether nucleation has occurred. Both the pipe and rock flow have conditions where nucleation likely can occur. We also look at the spinodal region where $\frac{\partial p}{\partial \rho} \le 0$ on the S-isotherms,[6] and note that within this region at the binodal pressure[7] is where a phase transition must occur.

[5] Fugacity is $\exp \int_0^p \left(\frac{dp'}{R_s T \rho(p',T)} - \frac{dp'}{p'} \right)$.

[6] "S" shaped because $(T,\cdot) \mapsto p$ has 3 roots ρ.

[7] The binodal isothermal saturation pressure and densities solve the 3 equations $p_s = p(T,\rho_g) = p(T,\rho_l) = \int_{\rho_g}^{\rho_l} p(T,\rho)\rho^{-2} d\rho / \left(\rho_g^{-1} - \rho_l^{-1}\right)$ derived from conservation of Gibbs free energy.

The pipe simulation uses ρ as the primary variable, so it is able to calculate up to the spinodal curve, inside the metastable region. The reservoir simulation uses p as the primary variable, so it cannot cover inside the metastable region, and the simulation stops when it hits the binodal region.

For both simulations, reaching the binodal region serves as a valid criterion for phase change since we are unlikely to have a metastable single-phase fluid given the likelihood of nucleation.

A.2 Reservoir Equations

MOOSE's reservoir simulation solves the PDE that consists of the following:

A.2.1 Mass Conservation

For water (phase 0):

$$\frac{\partial}{\partial t}\left(\phi\rho_0 S_0\right) + \nabla\cdot\left(\rho_0\mathbf{v}_0\right) = 0 \tag{A.69}$$

For CO_2 (phase 1):

$$\frac{\partial}{\partial t}\left(\phi\rho_1 S_1\right) + \nabla\cdot\left(\rho_1\mathbf{v}_1\right) = 0 \tag{A.70}$$

A.2.2 Darcy Velocity

$$\mathbf{v}_\beta = -\frac{k_{r\beta}}{\mu_\beta}K\left(\nabla P_\beta - \rho_\beta\mathbf{g}\right) \tag{A.71}$$

A.3 Heat Transport

$$\frac{\partial}{\partial t}\left[(1-\phi)\rho_r C_r T + \phi\sum_\beta S_\beta\rho_\beta C_\beta T\right] + \nabla\cdot\left(\sum_\beta \rho_\beta C_\beta T\mathbf{v}_\beta\right) = \nabla\cdot(\lambda_{eff}\nabla T) - \frac{2}{h}\sqrt{\frac{\lambda_a\rho_a C_a}{t}}(T-T_0) \tag{A.72}$$

A.4 Solid Mechanics

A.4.1 Effective Stress

$$\boldsymbol{\sigma}' = \boldsymbol{\sigma} - \alpha P_f\mathbf{I} \tag{A.73}$$

A.4.2 Hooke's Law

$$\boldsymbol{\sigma}' = \mathbf{C} : (\boldsymbol{\epsilon} - \beta(T - T_0)\mathbf{I}) \tag{A.74}$$

A.4.3 Momentum Balance

$$\nabla \cdot \boldsymbol{\sigma} + \rho_b \mathbf{g} = 0 \tag{A.75}$$

Symbol	Description
ϕ	Reservoir porosity
K	Permeability
μ_0	Water viscosity
μ_1	CO_2 viscosity
T_0	Initial temperature
P_0	Initial porepressure
α	Biot coefficient
λ_{dry}	Dry thermal conductivity
λ_{wet}	Wet thermal conductivity

Table A.1: Descriptions of variables for reservoir PDEs.

References

[1] T. LaForce, A. Mijic, J. Ennis-King, and L. Paterson. Semi-analytical solutions for nonisothermal fluid injection including heat loss from the reservoir: Part 2. Pressure and stress. *Advances in Water Resources*, 73:242–253, 2014b.

[2] Fabian Möller, Axel Liebscher, Sonja Martens, Cornelia Schmidt-Hattenberger, and Martin Streibel. Injection of CO_2 at ambient temperature conditions – pressure and temperature results of the "cold injection" experiment at the ketzin pilot site. *Energy Procedia*, 63:6289–6297, 2014. ISSN 1876-6102. doi:https://doi.org/10.1016/j.egypro.2014.11.660. URL https://www.sciencedirect.com/science/article/pii/S1876610214024758. 12th International Conference on Greenhouse Gas Control Technologies, GHGT-12.

[3] Hariharan Ramachandran. CO_2 Joule-Thomson coefficient. https://gitlab.com/haricage/co2-joule-thomson-coefficient, 2025. Accessed: 2025-04-13.

[4] Roland Span and Wolfgang Wagner. A new equation of state for carbon dioxide covering the fluid region from the triple-point temperature to 1100 K at pressures up to 800 MPa. *Journal of Physical and Chemical Reference Data*, 25(6):1509–1596, 11 1996. ISSN 0047-2689. doi:10.1063/1.555991. URL https://doi.org/10.1063/1.555991.

[5] L.G.H. (Bert) van der Meer, Cor Hofstee, and Bogdan Orlic. The fluid flow consequences of CO_2 migration from 1000 to 600 metres upon passing the critical conditions of CO_2. *Energy Procedia*, 1(1):3213–3220, 2009. ISSN 1876-6102. doi:https://doi.org/10.1016/j.egypro.2009.02.105. URL https://www.sciencedirect.com/science/article/pii/S1876610209007486. Greenhouse Gas Control Technologies 9.

[6] R. Von Mises, H. Geiringer, and G.S.S. Ludford. *Mathematical Theory of Compressible Fluid Flow*. Academic Press Inc., 1958. ISBN 9780486439419. URL https://books.google.com/books?id=UHIWh3RGVUkC.